Wireless ultrasonic wavefield imaging via laser for hidden damage detection inside a steel box

girder bridge

Wireless ultrasonic wavefield imaging via laser for hidden damage detection inside a steel box girder bridge

Yun-Kyu An[1], Homin Song[2] and Hoon Sohn[3]

[1] International Institute for Urban Systems Engineering, Southeast University, Nanjing, People's Republic of China
[2] Department of Civil and Environmental Engineering, University of Illinois at Urbana–Champaign, Urbana, IL 61801, USA
[3] Department of Civil and Environmental Engineering, Korea Advanced Institute of Science and Technology, Daejeon, South Korea

E-mail: hoonsohn@kaist.ac.kr

Abstract

This paper presents a wireless ultrasonic wavefield imaging (WUWI) technique for detecting hidden damage inside a steel box girder bridge. The proposed technique allows (1) complete wireless excitation of piezoelectric transducers and noncontact sensing of the corresponding responses using laser beams, (2) autonomous damage visualization without comparing against baseline data previously accumulated from the pristine condition of a target structure and (3) robust damage diagnosis even for real structures with complex structural geometries. First, a new WUWI hardware system was developed by integrating optoelectronic-based signal transmitting and receiving devices and a scanning laser Doppler vibrometer. Next, a damage visualization algorithm, self-referencing *f-k* filter (SRF), was introduced to isolate and visualize only crack-induced ultrasonic modes from measured ultrasonic wavefield images. Finally, the performance of the proposed technique was validated through hidden crack visualization at a decommissioned Ramp-G Bridge in South Korea. The experimental results reveal that the proposed technique instantaneously detects and successfully visualizes hidden cracks even in the complex structure of a real bridge.

Keywords: structural health monitoring, bridge field testing, ultrasonic wavefield imaging, wireless PZT excitation, laser Doppler vibrometer, self-referencing *f-k* filter, automated damage detection

(Some figures may appear in colour only in the online journal)

1. Introduction

Early damage detection of *in-situ* bridges gained significance after the cataclysmic collapse of several bridges, including collapse accidents at the Sungsoo Grand Bridge in South Korea in 1994; the Hintze Ribeiro Bridge in Portugal in 2001; the Minnesota I-35W Bridge in the USA in 2007; the Yangmingtan Bridge in China in 2012; the Washington State Bridge in the USA in 2013; and the Banghwa Bridge in South Korea in 2013. Many bridge collapse accidents have been initiated by local defects [1]. To date, a number of structural

health monitoring (SHM) techniques have been developed and applied to *in-situ* bridges for assessing their safety and integrity. For example, conventional vibration-based bridge monitoring techniques known as global SHM techniques are suitable for detecting changes in global dynamic characteristics such as natural frequencies and modal damping ratios. Although these conventional techniques are advantageous to evaluate the overall condition degradation of a target structure [2–4], they are often insensitive to local incipient damage in critical structural members [5, 6].

To surmount these limitations, a number of NDT techniques have been proposed, with attempts made to apply them to bridge damage detection: ultrasonic [7, 8], acoustic emission [9], eddy current [10] and magnetic inspection [11]. Compared to global SHM techniques, these local NDT techniques are sensitive to incipient damage, thus making it possible to prevent catastrophic failure of a bridge. Moreover, they potentially reduce the maintenance costs of a bridge by considering its life-cycle costs. Among the various NDT techniques, the ultrasonic technique has proven to be one of the most promising tools for bridge monitoring because ultrasonic waves are sensitive to local hidden damage and are capable of propagating over relatively long distances with little attenuation [8]. However, the ultrasonic technique confronts several technical challenges for field bridge monitoring: (1) sensor installation and cabling are labor-intensive and cumbersome because a huge number of sensors and electric cables are required for large area inspection, (2) spatially limited sensing points may not achieve enough spatial resolution to detect incipient damage, and (3) sensors and cables can be the weakest link in the bridge monitoring system, thus increasing long-term maintenance costs.

There are ongoing efforts to overcome the aforementioned technical challenges by using laser beams to generate and measure ultrasonic waves, which is called a laser ultrasonic technique. One of the most widely accepted principles of the laser ultrasonic technique is that ultrasonic waves are generated using a pulse laser, and the corresponding ultrasonic responses are measured by laser interferometry [12]. The laser ultrasonic technique has superior capability for local damage detection in that it can generate and measure ultrasonic waves in a noncontact way. Moreover, multi-dimensional ultrasonic wavefield images can be obtained by incorporating laser-scanning capability, enabling researchers to visualize structural damage with high spatial and temporal resolution. These features allow us to intuitively evaluate and instantaneously diagnose structural damage without relying on baseline data obtained from the undamaged condition of the target structure. Recently, complete noncontact laser ultrasonic wavefield imaging techniques have been developed for subsurface crack visualization in a metallic plate [13] and delamination/debonding visualization in composite structures [14].

Even though the laser ultrasonic technique has a number of advantages for damage detection, it still has technical limitations for the real field bridge application. First, noncontact ultrasonic wave generation using a pulse laser often has low efficiency on coated target surfaces. Note that bridge girder surfaces in South Korea are typically coated by thick paint layers for the purpose of maintenance. If the laser power is increased to generate a higher amplitude of ultrasonic waves, surface ablation occurs due to the coated paint's low melting temperature. Second, laser-generated ultrasonic waves most likely become surface waves at the near field of the incident laser source. However, because these surface waves are not sensitive to subsurface damage, far-field responses with higher amplitudes are required for subsurface damage detection. Unfortunately, the distance between laser excitation and sensing points is often limited because laser-generated ultrasonic waves have relatively low amplitudes compared to the inherently high noise level in the bridge field. For these reasons, a new wireless ultrasonic generation system incorporated with a wireless piezoelectric transducer (PZT) rather than the complete noncontact ultrasonic excitation system using a pulse laser was developed and applied to the real bridge in this study.

Recently, a number of wireless ultrasonic techniques have been developed to overcome the drawbacks of the conventional wired ultrasonic techniques. One of the most noticeable achievements is the development of a wireless transducer node based on radio frequency (RF) technology [15, 16]. The RF node wirelessly carries the desired ultrasonic excitation and sensing signals through radio waves in the frequency range of several hundred MHz. However, additional power supplies from solid-state batteries or power harvesting devices are required for their uninterrupted operation. This additional power supply potentially increases long-term maintenance costs associated with the battery replacement and repair. Alternatively, an inductively coupled ultrasonic transducer has been proposed [17]. Although additional power sources are not necessary, the transmission distance for wireless power and data transmission is limited in the order of centimeters. More recently, laser-based wireless ultrasonic generation and measurement systems have been developed by [18]. The main advantages of the laser-based wireless system are that (1) the excitation laser beam can wirelessly provide the desired ultrasonic waveforms as well as the required power for ultrasonic excitation, and (2) the transmission distance between the laser source and the target excitation or sensing node can be more than several meters.

This study proposes a novel wireless ultrasonic wavefield imaging (WUWI) system where a surface-mounted PZT is wirelessly excited by a modulated laser beam, and the corresponding ultrasonic responses are measured by scanning with a laser Doppler vibrometer (LDV). Then, a damage visualization algorithm, called a self-referencing *f-k* filter (SRF), is introduced [19] to automatically identify and localize hidden cracks. The proposed system and algorithm are then applied to the decommissioned Ramp-G Bridge in South Korea, which is a unique opportunity for destructive testing in a real bridge structure.

This paper organized as follows. First, the hardware development for the WUWI system is described in section 2, and the details of the SRF are explained in section 3. Next, the applicability of the proposed technique to a real bridge structure is examined by destructive testing of the Ramp-G Bridge in sections 4 and 5. Finally, this paper concludes with summary and discussion in section 6.

2. Hardware development of a WUWI system

The proposed WUWI system is composed of excitation, sensing and control units, as well as a PZT excitation node, as shown in figure 1. The working principle of the WUWI system is as follows. First, the virtual grid points for scanning
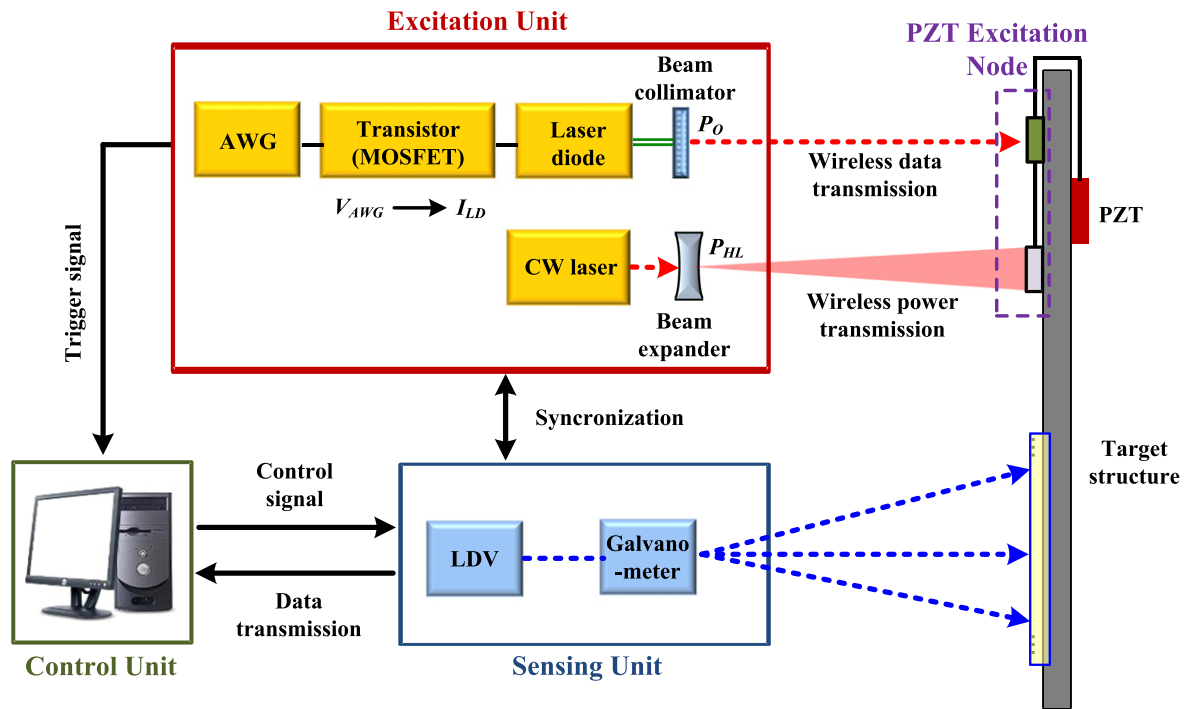
Figure 1. Schematic diagram of a WUWI system composed of excitation, sensing and control units, as well as a PZT excitation node.

and sensing are created on the target surface using a digital camera and a software program embedded in the control unit. Subsequently, the sequences of scanning sensing points are predetermined. Once the grid points and scanning sensing sequences are determined, an arbitrary waveform generator (AWG) in the excitation unit sends out a trigger signal to the control unit to activate the synchronized excitation and sensing. Next, the control signal from the control unit is transmitted to the sensing unit for data acquisition. In the excitation unit, an arbitrary electric voltage signal is generated and converted into a laser beam by a laser diode, and the laser beam is wirelessly transmitted to a photodiode in the PZT excitation node. Then, the photodiode reconverts the optical signal into an electric voltage signal so that the PZT embedded in the target structure is excited, and ultrasonic waves are consequently generated. Here, the power required to operate the PZT excitation node is supplied by an additional high-power laser in the excitation unit, as shown in figure 1. The corresponding ultrasonic responses are measured at the first predetermined measurement point, and the measured data are transmitted to the control unit for signal processing. The control unit consecutively moves the sensing laser beam automatically to the next measurement point by sending control signals to the sensing unit. By repeating the prescribed procedure over the predetermined sensing points, ultrasonic wavefield images are constructed onto the target surface and processed to automatically visualize hidden damage.
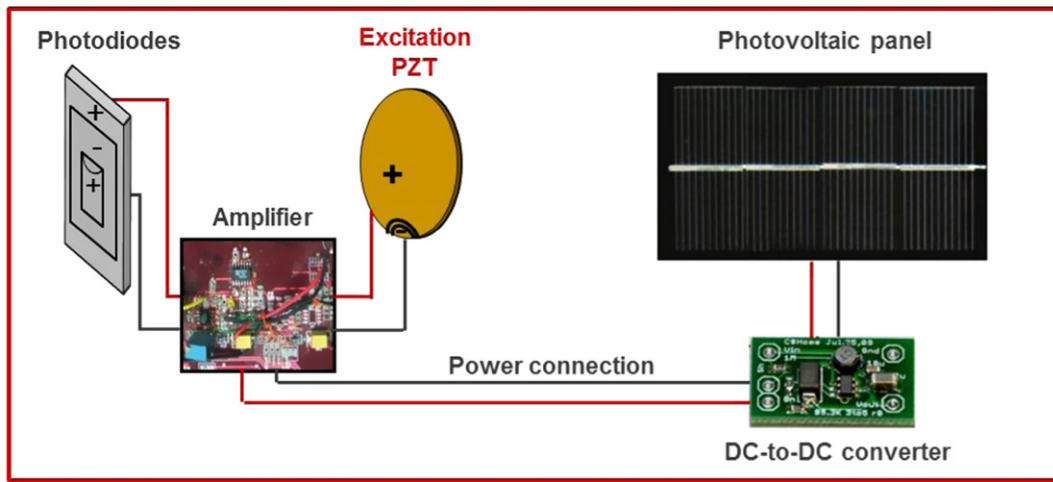
2.1. Excitation unit and PZT excitation node

The excitation unit is divided into a laser signal transmission part and a wireless power transmission part, as shown in

figure 1. The laser signal transmission part consists of AWG, a transistor, a laser diode and a beam collimator, and the wireless power transmission part is composed of a high-power laser and a beam expander [18]. First, a desired voltage input (V_{AWG}) such as a toneburst signal is generated by AWG and applied to the transistor which amplifies and controls electric signals. Here, a metal-oxide-semiconductor field-effect transistor (MOSFET) is used in this study because it can effectively control an output current by an input voltage [20]. Then, the transistor, where V_{AWG} is applied, creates a modulated current signal (I_{LD}), and I_{LD} is subsequently applied to the laser diode. The laser diode (LPSC-1310-FC, Thorlabs Inc.) transmits the modulated laser signal (P_O) to the beam collimator through an optical fiber, and P_O is emitted to a photodiode in the PZT excitation node. Here, V_{AWG} needs to have a dc offset voltage because P_O can have only positive values. Note also that there is a nonlinear relationship between V_{AWG} and P_O that can distort the original waveform of V_{AWG} due to the nonlinear characteristics of the transistor and the laser diode [21]. To reduce such nonlinear effects, the peak-to-peak amplitude of V_{AWG} is limited within a small range of around 300 mV in this study.

To operate the PZT excitation node, a certain level of electrical power is necessary. Here, the high-power laser (15 W, 532 nm) in the excitation unit wirelessly transmits the required power to the PZT excitation node. The high-power laser beam (P_{HL}) is transmitted to the beam expander, and P_{HL} is emitted to the photovoltaic panel in the PZT excitation node, as shown in figure 1.

The PZT excitation node is further divided into a PZT excitation part and an electric power supply part. The PZT excitation part is composed of a photodiode (FDG1010, Thorlabs Inc.), an amplifier and a PZT installed in the target

(a)
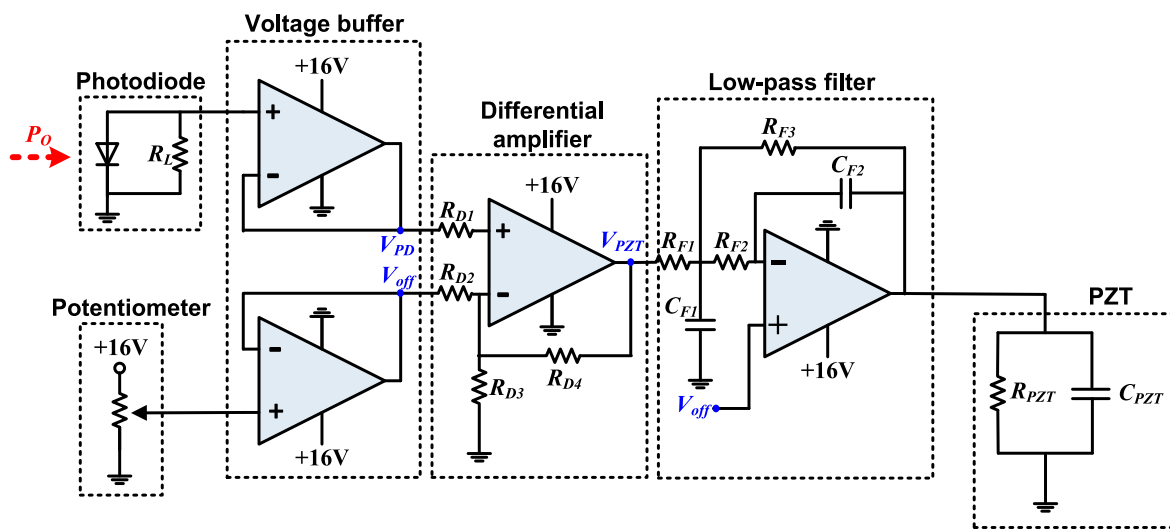
(b)

Figure 2. Wireless PZT excitation node: (a) the overall composition and (b) the amplifier's schematic circuit diagram.

structure. Then, the electric power supply part is comprised of a photovoltaic panel (M165110, Solarcenter Inc.) and a dc-to-dc converter (LM7815CT, Fairchild Semiconductor Inc.) that supplies electric power to the amplifier, as shown in figure 2(a). The working principle for the PZT excitation node is as follows. The P_O is reconverted into the current source (I_{PD}) by the photodiode in the PZT excitation node. Here, I_{PD} is linearly proportional to P_O, and the output voltage (V_{PD}) produced by the photodiode is given as [22]:

$$V_{PD} = \frac{nk_B T}{e} \ln\left(\frac{I_{PD}}{I_r} + 1\right) \qquad (1)$$

where I_r is the reverse saturation current, e is an electron charge (-1.60×10^{-19} C), k_B is Boltzmann's constant (8.61 μeV/K), T is the absolute temperature of the photodiode and n is the ideality factor, depending on the semiconductor material and fabrication characteristics ($n = 1$–2).

Next, the amplifier shown in figure 2(b) is used to magnify V_{PD} into V_{PZT} because the V_{PD} level is not high

enough to excite a typical PZT transducer mounted on a real structure. The electric circuit structure of the PZT excitation node (except the low-pass filtering part) is identical to the one described in [19], and the power supply voltage of the operational amplifiers in this study is 16 V, resulting in 16 V being the maximum magnifying capacity of the amplifier. To reduce high-frequency electrical noise components, a newly designed low-pass filter is embedded between the differential amplifier and the excitation PZT, as shown in figure 2(b). The cut-off frequency ($f_{cut\text{-}off}$) and the gain factor (G) of the low-pass filter are adjusted to be 215 kHz and −2, respectively, by setting the resistor values R_{F1}, R_{F2} and R_{F3} to 500, 500 and 1000 Ω, respectively, and the capacitor values C_{F1} and C_{F2} to 500 and 2200 pF, respectively. $f_{cut\text{-}off}$ and G of the low-pass filter can be computed as:

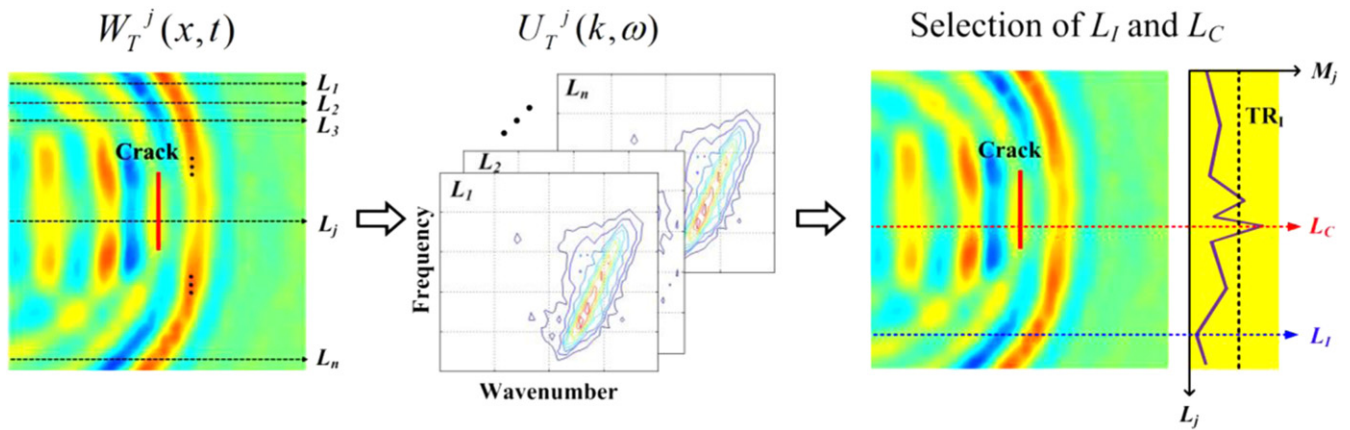$$f_{cut-off} = \frac{1}{2\pi\sqrt{R_{F2}R_{F3}C_{F1}C_{F2}}} \qquad (2)$$

Figure 3. Selection of scanning lines L_C and L_I: L_j is the the jth scanning line parallel to the incident wave propagation direction. L_j is designated to be L_C when the M_j value defined in equation (5) becomes the maximum for L_j among all scanning lines. L_j becomes L_I when it has the minimum M_j value.

$$G = -\frac{R_{F3}}{R_{F1}} \quad (3)$$

As described in the previous subsection, the power required to operate the PZT excitation node is wirelessly transmitted by the high-power laser in the excitation unit. Once P_{HL} is emitted to the photovoltaic panel in the PZT excitation node, it converts the input laser power into electrical power. The dc-to-dc converter, which can regulate the output voltage level of 16 V, is used to supply stable electrical power to the amplifier. Here, the maximum PZT excitation voltage (V_{PZTmax}) of 14 V can be obtained when the converted electrical power is equal to or larger than 240 mW.

2.2. Sensing unit

A commercial scanning LDV (PSV-400-M4, Polytec Inc.) with a built-in galvanometer and an auto-focal lens [23] is used for the sensing unit. The LDV measures the out-of-plane velocity in the range from 0.01 μm/s to 10 μm/s onto a target surface based on the Doppler frequency-shift effect of light. To further illustrate, the LDV computes the frequency shift of the laser beam reflected from a vibrating target surface from its interference with a reference laser beam [12]. The laser source used for the LDV is a helium–neon (He-Ne) laser with a wavelength of 633 nm, and the optimal measurement distance is at $99 + 204n$ (mm), where n denotes an integer number. Then, the minimum focal length of the auto-focal lens is 0.35 mm, and the velocity sensitivity is 10 mm/s/V. The galvanometer embedded in the LDV allows a maximum rotating speed of 5730°/s and an angular resolution of 6.6×10^{-4}°. Note that the measurement sensitivity of the LDV highly depends on the target surface's condition, so a special surface treatment is often required to enhance measurement sensitivity from a rough surface.

2.3. Control unit

The control unit is composed of a personal computer (PC), a controller, a velocity decoder with a maximum velocity

sensitivity of 1 mm/s/V and a 14-bit digitizer with a maximum sampling frequency of 5.12 MHz. First, AWG in the excitation unit sends out the trigger signal when it produces V_{AWG}. Then, the controller subsequently sends out the control signal to the sensing unit to simultaneously start data collection. The velocity decoder computes the out-of-plane velocity by relating it to the frequency shift of the laser beam reflected from the target surface based on the Doppler effect. Once the ultrasonic wave responses are collected at multiple measurement points over the target structure, the corresponding ultrasonic wavefield images are constructed using MATLAB® codes developed in this study and stored on the PC.

3. Self-referencing *f-k* filter (SRF) for automated crack detection

In this section, SRF is introduced so that crack-induced ultrasonic modes are solely isolated from the measured ultrasonic wavefield (W_T). The feasibility of SRF has already been successfully verified in a well-controlled laboratory environment [19], and its real-field applicability is now being further investigated in a full-scale bridge structure in this study.

The main advantage of SRF lies in that it can extract only crack-induced ultrasonic modes even when they are all mixed with multiple ultrasonic modes produced by additional structural complexities such as stiffeners, holes and thickness variation. Moreover, the filtering parameters of SRF are determined using W_T obtained from only the current state of a target structure, rendering it to instantaneously evaluate cracks without any prior baseline wavefield image, called baseline-free damage diagnosis. These attractive features of SRF enhance its applicability to an existing bridge. Once W_T is measured from the entire scanning area using the WUWI system, SRF is applied according to the following steps.

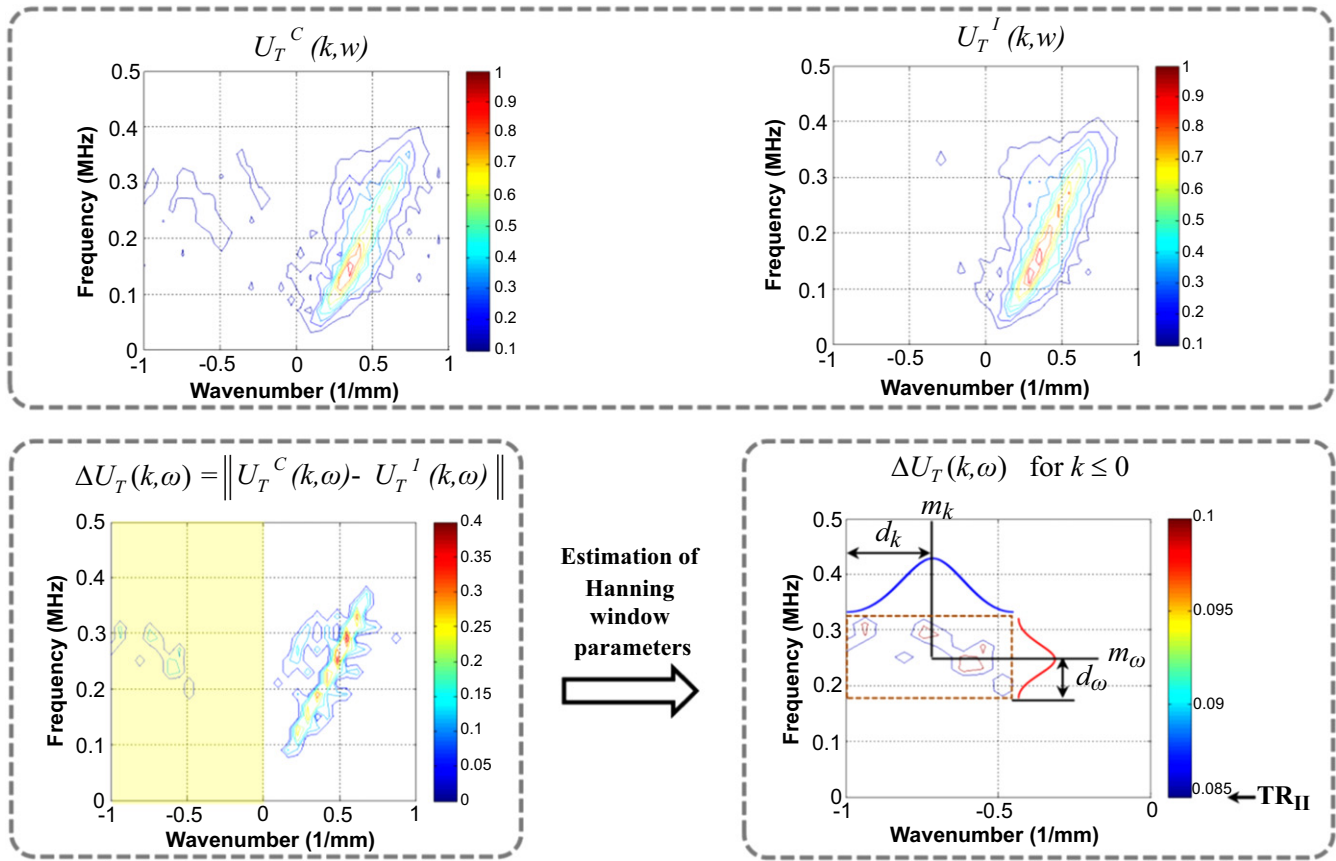(1) Transformation of the ultrasonic wavefield signals from the time–space (t–s) domain to the frequency–

Figure 4. Determination of Hanning window filtering parameters. Once L_C and L_I are selected, the filtering parameters are determined so that the difference between U_T^C and U_T^I in equation (3) can be highlighted in the region of $k \leqslant 0$.

wavenumber (*f–k*) domain along multiple scanning lines parallel to the incident wave propagation direction.

To begin with SRF, it is assumed that the crack is spatially limited to a small area within the scanning area. After W_T is obtained from the entire scanning area in the *t–s* domain, multiple scanning lines parallel to the ultrasonic wave propagating direction are chosen, as shown in figure 3. Here, L_j denotes the *j*th scanning line where $j = 1$ to n. Then, the ultrasonic wavefields corresponding to L_j are transformed from the *t–s* domain to the *f-k* domain using the 2D Fourier transform (2D FT):

$$U_T^j(k, \omega) = \int_{-\infty}^{\infty} \int_{-\infty}^{\infty} W_T^j(x, t) \, e^{-i(kx+\omega t)} \, dx dt \qquad (4)$$

where W_T^j and U_T^j denote the ultrasonic wavefields along L_j in the *t–s* and *f–k* domains, respectively, and k, x, ω and t denote the wavenumber, spatial coordinate, angular frequency and time, respectively.

(2) Selection of two scanning lines crossing the intact and damaged areas from the entire scanning area.

In this step, the existence of a crack is first determined, and then the representative two scanning lines, L_I and L_C crossing both the intact and cracked areas, respectively, are selected through the subsequent procedure. Once U_T^j is computed from equation (4), the maximum difference (M_j) between two adjacent U_T^j and U_T^{j+1} is computed with respect to k and ω:

$$M_j = \max \| U_T^j(k, \omega) - U_T^{j+1}(k, \omega) \|$$
$$\forall \; \omega, \; k \leqslant 0 \text{ and } j = 1 \text{ to } n - 1 \qquad (5)$$

where 'max' operator means the selection of the maximum value with respect to absolute difference values between adjacent wavefields in the *f–k* domain. Note that the domain for k is restricted to $k \leqslant 0$ so as to only consider the ultrasonic waves reflected from the crack and propagating opposite to the incident ultrasonic waves.

Next, once M_j values are computed for $j = 1$ to $n - 1$, their probability density function (PDF) is estimated by fitting a Type III extreme value distribution called a Weibull distribution to all M_j values. Subsequently, a threshold value (TR$_I$) with respect to a one-sided 95% confidence interval is calculated. Consequently, the crack existence is identified when any M_j value exceeds TR$_I$. Then, L_j's corresponding to the maximum and minimum M_j values are chosen as L_I and L_C, respectively, as shown in figure 3. The physical premise of this L_I and L_C selection procedure is that ultrasonic wave signals obtained from the adjacent intact scanning lines will not be changed much when spatial scanning resolution is small, but they will be drastically altered by a crack formation even though the target area is densely scanned.

(3) Determination of Hanning window parameters for SRF.

(a)

(b)

Figure 5. Decommissioned Ramp-G Bridge in Goyang, Gyunggi, Korea: (a) overview and (b) bottom view. Curved 90 m-long Ramp-G Bridge has two steel box girders.
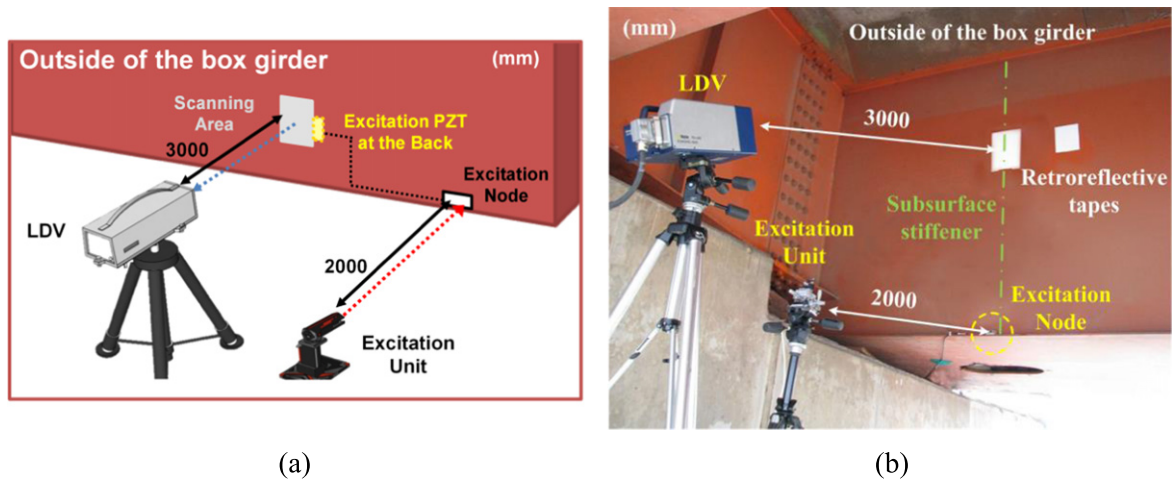

(a)

(b)

Figure 6. Experimental setup for subsurface-crack detection in an *in-situ* bridge: (a) a schematic view and (b) real field view. Excitation PZTs and artificial cracks are located on the opposite side (inside the box girder) of the scanning areas.

Once L_I and L_C are selected, the parameters of the following two Hanning windows are estimated for the subsequent f–k filtering. Φ_k in the k domain and Φ_ω in the f domain are defined, respectively, as:

$$\Phi_k = \begin{cases} 0 & |k - m_k| > 2d_k \\ 0.5 + 0.5\cos\left[\dfrac{\pi(k - m_k)}{d_k}\right] & |k - m_k| \leqslant 2d_k \end{cases} \quad \forall\, \omega \quad (6)$$

$$\Phi_\omega = \begin{cases} 0 & |\omega - m_\omega| > 2d_\omega \\ 0.5 + 0.5\cos\left[\dfrac{\pi(\omega - m_\omega)}{d_\omega}\right] & |\omega - m_\omega| \leqslant 2d_\omega \end{cases}$$
$$\text{for } k \leqslant 0 \quad (7)$$

where m_k and $2d_k$ denote the center and width of Φ_k at a given ω, respectively, and m_ω and $2d_\omega$ denote the center and width of Φ_ω at a given k, respectively.

Here, the appropriate selection of the center and width parameters of Φ_k and Φ_ω is critical to the performance of SRF isolating the crack-induced features. Figure 4 shows the

successive procedure for determining these center and width parameters. First, the parameter determination starts with the calculation of the difference (ΔU_T) between U_T^C and U_T^I, which are the f–k domain ultrasonic wavefields corresponding to L_I and L_C, respectively:

$$\Delta U_T(k, \omega) = \| U_T^C(k, \omega) - U_T^I(k, \omega) \| \qquad \text{for } k \leqslant 0 \quad (8)$$

ΔU_T contains noise components as well as crack-induced features. To isolate only the crack-induced ultrasonic modes, the PDF of ΔU_T is estimated by fitting a Type I extreme value distribution, known as a Gumbel distribution, to all entities in ΔU_T for $k \leqslant 0$, and then a threshold value (TR$_{II}$) corresponding to a 95% confidence interval is computed. Then, the ΔU_T values above TR$_{II}$ are retained in the f–k domain plot. Once the retained ΔU_T values are projected onto the k domain, the maximum and minimum k values are calculated. Afterwards, m_k is selected as the mean value between the maximum and minimum k values, and $2d_k$ the difference between the maximum and minimum k values, as shown in figure 4. In a similar fashion, m_ω and $2d_\omega$ are determined in the f domain.
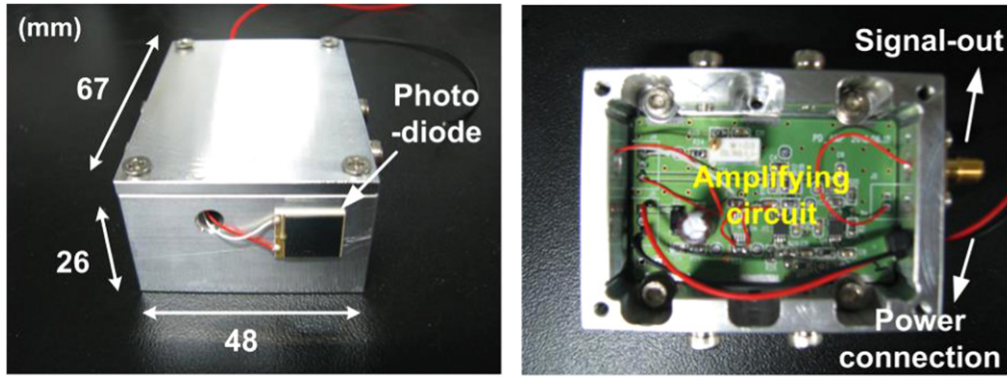
Figure 7. Prototype of the wireless PZT excitation node including a photodiode and an amplifying circuit.
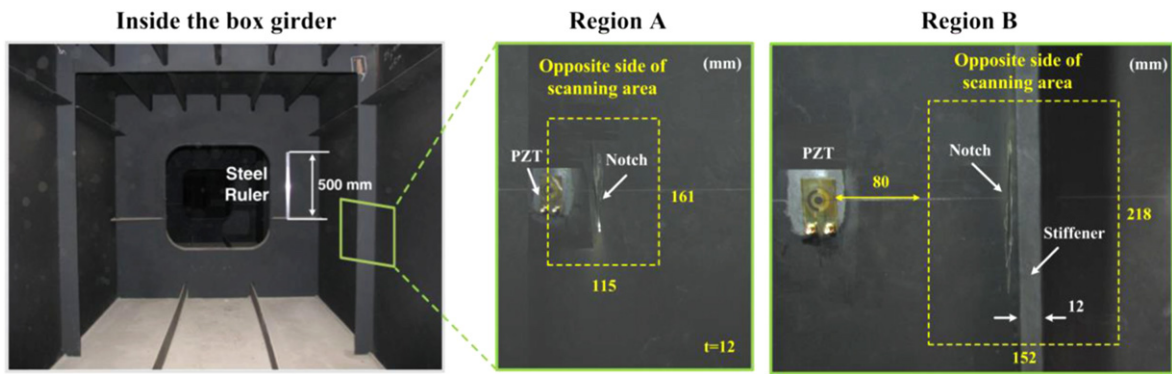

Figure 8. Inside view of the steel box girder, PZT installation and introduced notches: Regions A and B represent flat and stiffened scanning areas, respectively.
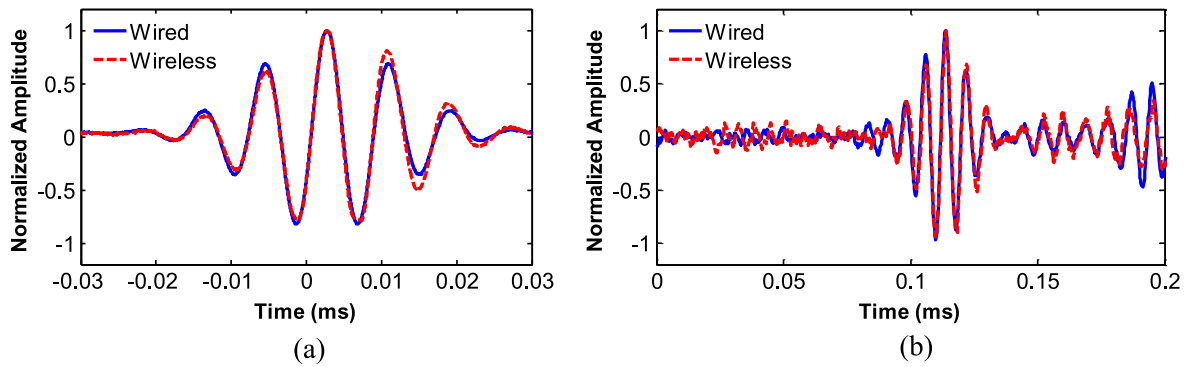

Figure 9. Comparison of input and output signals obtained by wired and wireless PZT excitations: (a) Wired and wireless mean the input signals generated by AWG and wirelessly transmitted to the excitation node, respectively. (b) Wired and wireless outputs represent the corresponding output response signals measured by an LDV.

(4) Isolation of crack-induced ultrasonic modes through self-referencing *f-k* filtering.

Now, a filtered ultrasonic wavefield (U_F^j) corresponding to L_j is obtained by:

$$U_F^j(k, \omega) = U_T^j(k, \omega) \cdot \varPhi_k(k) \cdot \varPhi_\omega(\omega)$$
$$\forall \, \omega, \, k \leqslant 0 \text{ and } j = 1 \text{ to } n - 1 \qquad (9)$$

Consequently, the resultant ultrasonic wavefield (W_F^j) according to L_j in the *t–s* domain is reconstructed by an

inverse 2D FT:

$$W_F^j(x, t) = \frac{1}{2\pi} \int_{-\infty}^{\infty} \int_{-\infty}^{\infty} U_F^j(k, \omega) e^{i(kx+\omega t)} dk d\omega \qquad (10)$$

The cumulative energy of W_F^j can be computed as:

$$E_F^j(x, t) = \int_0^t \left[W_F^j(x, t) \right]^2 dt \qquad (11)$$

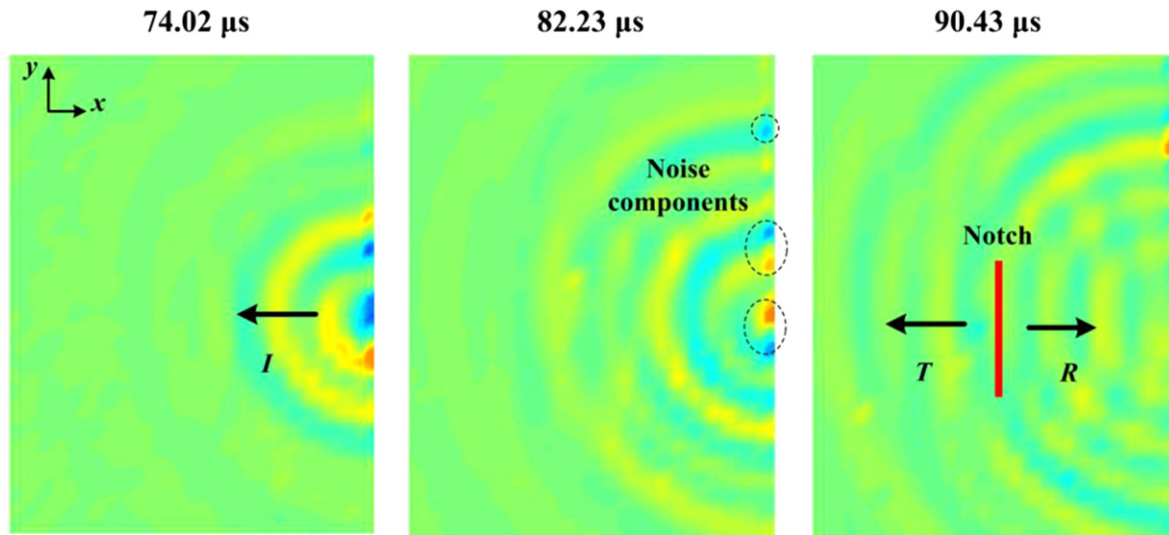where $E_F^j(x, t)$ represents the energy of W_F^j cumulated up to a

8

Figure 10. Representative ultrasonic wavefield images obtained at Region A using the WUWI system: *I*, *T* and *R* denote incident, transmitted and reflected waves, respectively.

time point of *t*. In a similar manner, $E_T^j(x, t)$ can be calculated from equation (11) using W_T^j instead of W_F^j.

Once E_F^j values are obtained over the whole L_j's, the E_F image in the 2D spatial domain is constructed by assembling all E_F^j plots. Note that only the crack formation is highlighted in E_F image and the rest of the ultrasonic modes are de-emphasized, because SRF acts as a band-pass filter for isolating the crack-induced ultrasonic modes.

(1) Denoising based on extreme value statistics:

To obtain further clear resultant images, an additional denoising process is performed by employing a threshold value (TR_{III}) based on extreme value statistics with respect to the E_F [24]. First, the PDF of all $E_F^j(x, t)$ data is estimated by fitting the Weibull distribution. Then, TR_{III} corresponding to a one-sided 97% confidence interval is computed. After denoising, only $E_F^j(x, t)$ values exceeding TR_{III} are retained, resulting in only a crack-induced ultrasonic mode image.

4. Description of field bridge test

To examine the applicability of the proposed technique to a real bridge structure, a series of full-scale field tests were conducted at a decommissioned bridge, the Ramp-G Bridge, in Goyang, Kyunggi, South Korea. Figure 5 shows that Ramp-G Bridge is a curved double-span bridge composed of a concrete deck and two steel box girders. The inspected area is located near one of the abutments of the bridge, as shown in figure 5(a). Although this bridge is already decommissioned, it undergoes perceptible ambient vibrations due to its closeness to nearby heavy traffic and wind loads.

The wireless PZT excitation node is embedded inside the steel bridge girder for ultrasonic generation, and corresponding responses are measured by the LDV scanning on the outer surface of the box girder. Figure 6 shows the field test
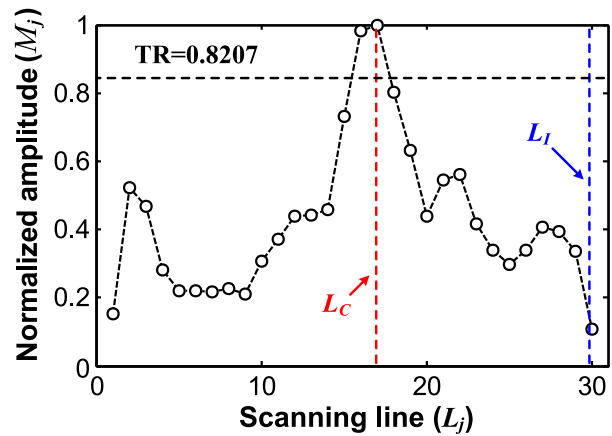

Figure 11. Selection of L_C and L_I, which denote the scanning lines corresponding to the maximum and minimum M_j values, respectively.

setup of the WUWI system outside the box girder. The excitation unit is 2 m apart from the excitation node installed on the outer surface of the box girder, as shown in figure 6. Then, the distance between the LDV and the target surface is approximately 3 m. To improve the sensitivity of the LDV, retro-reflective tapes are used on the scanning surface. Here, the PZT excitation node is connected to the PZTs embedded on the inner surface of the box girder.

Figure 7 shows the prototype of the wireless PZT excitation node. A photodiode and the amplifying circuit designed in this study are packaged inside an aluminum case so that external physical and electrical disturbances can be avoided during field-testing. In this field test, the converted electrical power of 240 mW is necessary to obtain V_{PZTmax} of 14 V.

Next, the experimental setup inside the box girder is shown in figure 8. Two different target areas, Regions A and B, are inspected. Region A is a flat region with no additional
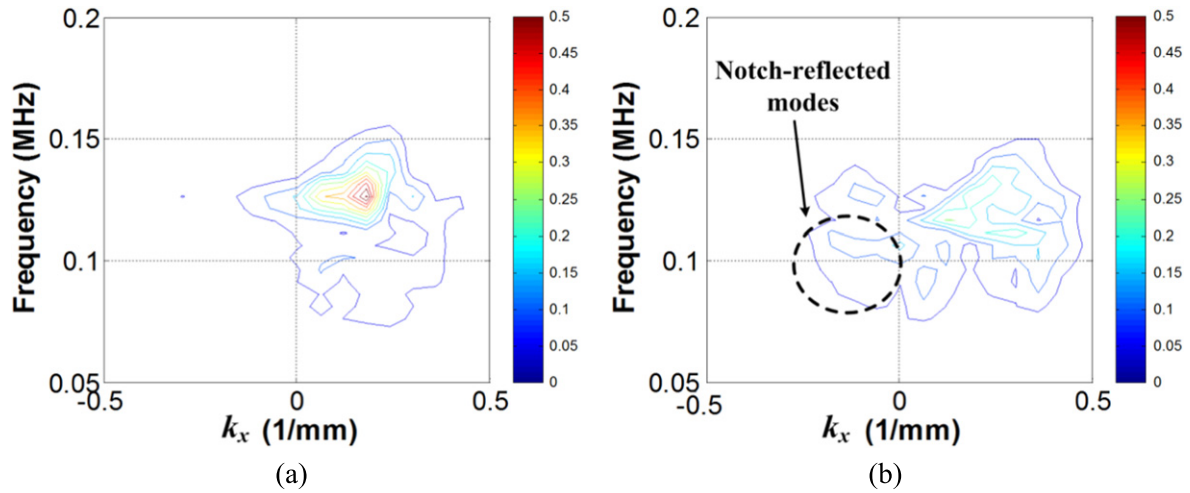
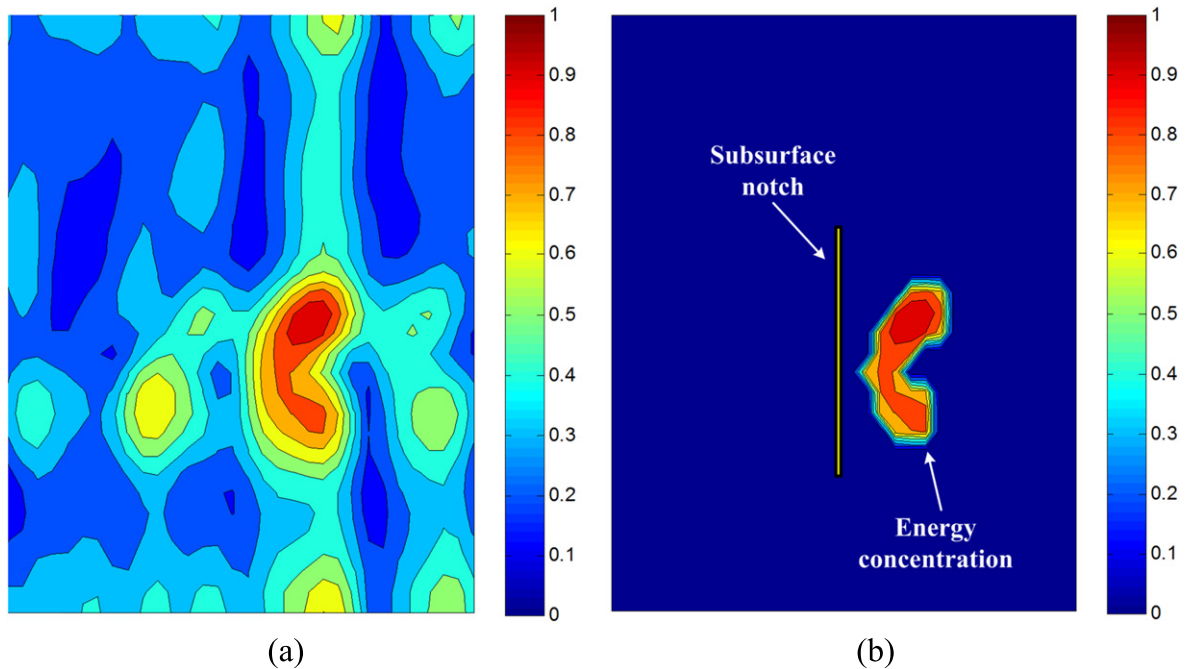**Figure 12.** The *f–k* domain plots obtained at Region A: (a) U_T^I and (b) U_T^C.

Figure 13. E_F images obtained at Region A (115×161 mm^2): (a) before and (b) after denoising.

structural features, and Region B is a stiffened region with a vertical stiffener inside the box girder. Again, because the LDV scans only cover each region of the box girder's outer surface, as shown in figure 6, additional structural boundaries cannot be observed on the scanning surface. The scanning areas of Regions A and B are, respectively, 115×161 mm^2 and 152×218 mm^2, and the spatial resolutions of each region are set to 5 mm and 3 mm, respectively.

The PZT used for ultrasonic wave generation is an APC 850 type [25] with a diameter of 18 mm and a thickness of 0.508 mm, which is specially designed by encapsulating Kapton tapes with printed circuits and SMA connectors to improve their durability against harsh environments and to make their installations easier. For effective PZT placements,

the protective paint layer is stripped off at the PZT positions using sandpaper, and extra care is taken to control the thickness of the bonding layer to be uniform. Then, artificial notches are introduced in both regions: an 80 mm-long, 4 mm-deep and 1 mm-wide notch in Region A, and a 100 mm-long, 4 mm-deep and 1 mm-wide notch in Region B, as shown in figure 8. Note that the notch reasonably represents a crack if the width of the notch is significantly smaller than the wavelength of the ultrasonic waves [26]. Here, the depths of both notches are 30% of the bridge girder thickness of 12 mm. Note that the notches (hereafter called subsurface notches) introduced in both regions cannot be observed outside the box girder. Even if the PZTs are attached to the outside of the box girder, the notches can be sufficiently
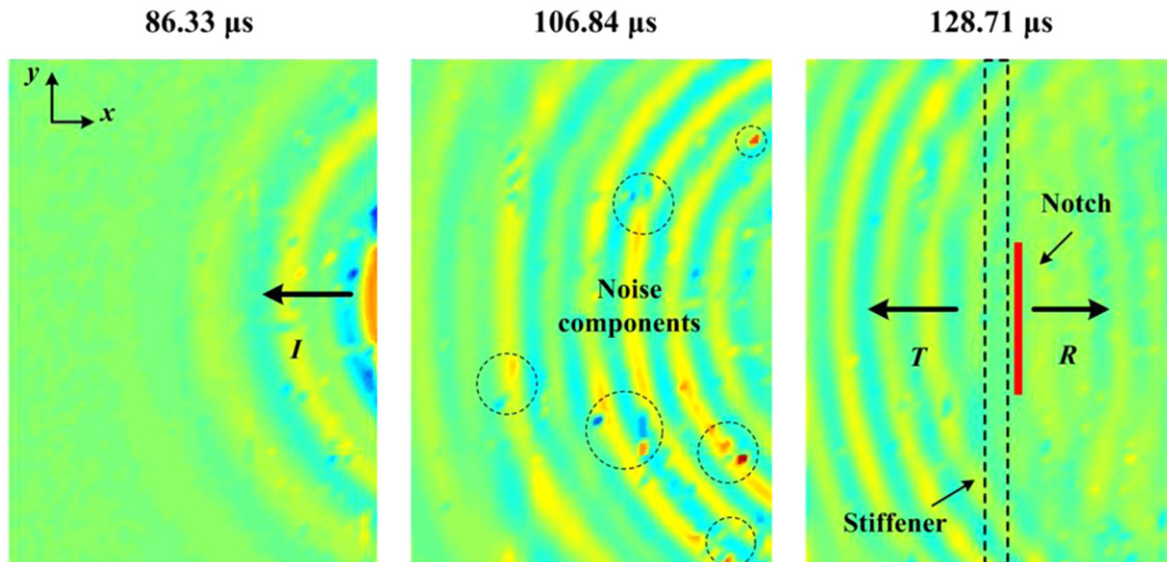
Figure 14. Representative ultrasonic wavefield images obtained at Region B using the WUWI system: *I*, *T* and *R* denote incident, transmitted and reflected waves, respectively.
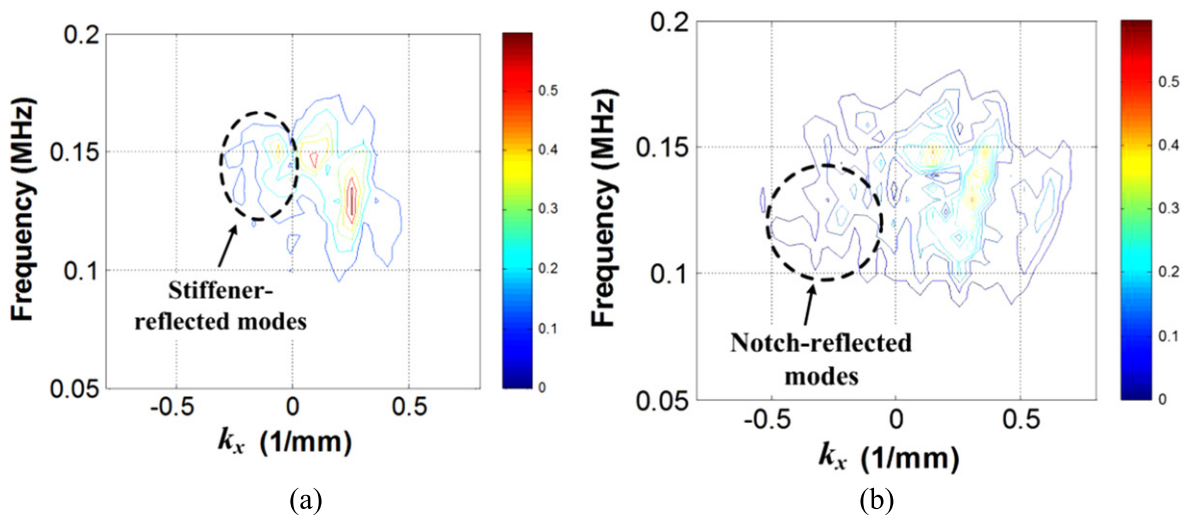

Figure 15. The *f–k* domain plots obtained at Region B: (a) U_T^I and (b) U_T^C.

detected. In this study, the PZTs are installed inside the box girder to minimize the long-term degradation of the PZTs due to harsh outdoor environments.

Seven-cycle toneburst input signals with a driving frequency of 130 kHz and a peak-to-peak voltage level of 14 V are applied to the PZTs using the wireless PZT excitation node, and the corresponding responses are scanned by an LDV with a sampling frequency of 5.12 MHz. The sensitivity of the velocity measurement is set to 10 mm/s/V. Then, the response signals at each sensing point are measured 100 times and averaged in the time domain to enhance the signal-to-noise ratio. Moreover, a low-pass filter in the PZT excitation node with its $f_{cut\text{-}off}$ of 215 kHz removes unwanted responses outside the frequency range of interest.

5. Field test results

5.1. Preliminary test

To examine the performance of the wireless PZT excitation, preliminary tests were performed before crack detection tests using the WUWI system. Figure 9 compares the input and output signals obtained by wired and wireless PZT excitation approaches. Here, the wired approach denotes that a PZT is excited by AWG directly connected to a PZT using an electric wire. Each signal is normalized by its maximum amplitude. Close agreement between the two input signals obtained from the wired and wireless PZT excitation approaches is observed in figure 9(a), although little distortion of the input waveform exists. Then, the corresponding responses measured at a
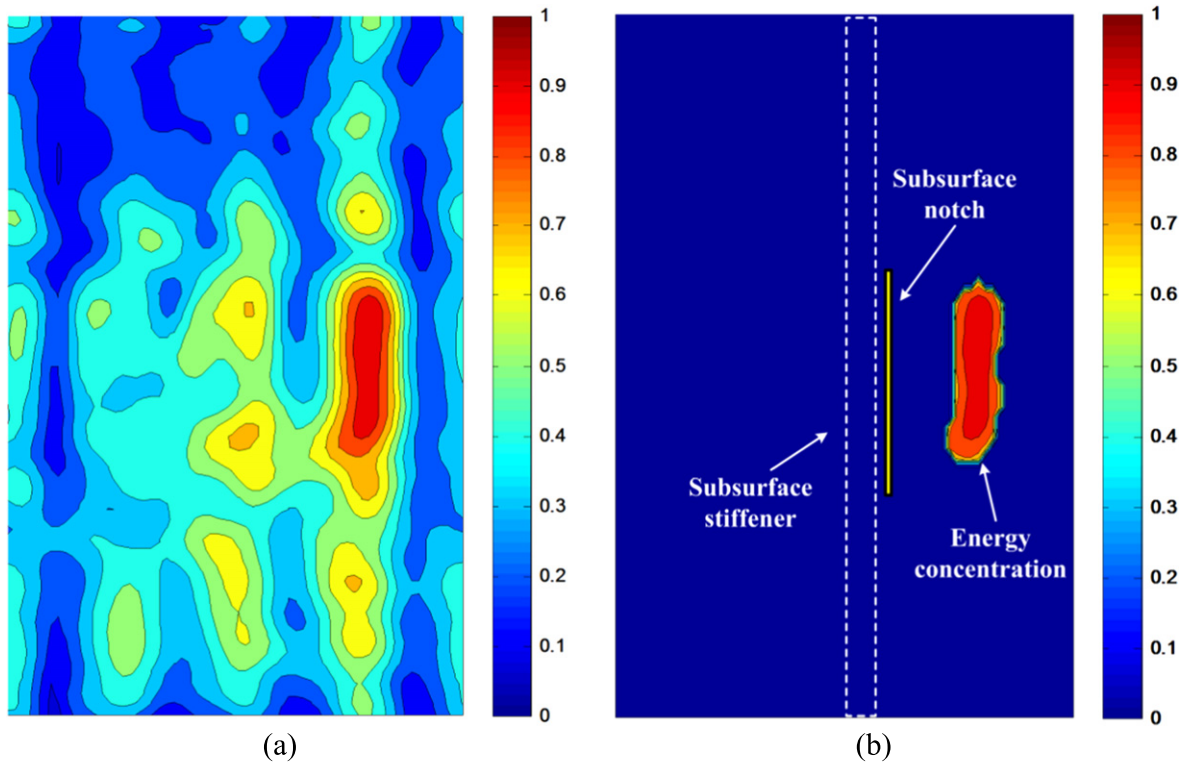
Figure 16. E_F images obtained at Region B (152×218 mm^2): (a) before and (b) after denoising.

specific spatial point using an LDV are also compared in figure 9(b), revealing that the wireless PZT excitation node properly generates ultrasonic waves.

5.2. Hidden crack detection in region A

Figure 10 displays representative ultrasonic wavefield images obtained in Region A using the WUWI system. At 74.02 μs, only incident waves (I) can be observed, and then transmitted (T) and reflected waves (R) from the notch are clearly observed at around 90 μs. Here, spatial averaging was performed to reduce the noise components caused by the high irregularity of the bridge surface. Assuming that the spatial resolution of the scanning measurement is sufficiently small, the discrepancies among adjacent points can be negligible.

Now, the SRF described in section 3 is applied to isolate the weak R generated from the subsurface notch. The M_j values calculated along the y-axis in figure 10 using equation (5) are displayed in figure 11. Based on the L_I and L_C selection procedure described in section 3, TR of Region A is computed as 0.8207 and L_{30} and L_{17} are respectively chosen as L_I and L_C, as shown in figure 11. Next, the corresponding U_T^I and U_T^C are shown in figures 12(a) and (b), respectively. Although reflected modes should not be theoretically observed in figure 12(a), weak reflected modes exist because of unwanted noise components. However, the perceptible notch-reflected modes are clearly visualized in figure 12(b), even though their amplitudes are much smaller than those of the transmitted modes.

Based on the computed filtering parameters explained in section 3, the E_F images are obtained by assembling all E_F^j

values, as shown in figure 13. Figure 13(a) shows that the energy of the notch-reflected modes was well extracted and concentrated in front of the subsurface notch. To further identify and localize the notch, the denoising process described in step (5) of section 3 was carried out. Consequently, the final resultant image of figure 13(b) shows that only the notch-induced mode energy was emphasized after the denoising process, making it possible to identify and localize the subsurface notch without relying on any baseline data previously obtained from the pristine condition of the bridge structure.

5.3. Hidden crack detection in region B

Similarly, figure 14 shows ultrasonic wavefield images obtained from Region B. Similar wave propagation patterns can be observed in figure 10 except the difference in that R comes from the vertical stiffener as well as the subsurface notch. Here, more discernable noise components are observed in figure 14 compared to figure 10 due to higher surface irregularity.

In a similar fashion to the previous results of Region A, L_I and L_C of Region B are determined as L_{68} and L_{23}, and the corresponding U_T^I and U_T^C are shown in figures 15(a) and (b), respectively. Similar results obtained in Region A can be observed, but clearer stiffener-reflected modes are revealed in figure 15(a). Although the notch-reflected modes coexist with the stiffener-reflected modes, remarkably distinguishable notch-reflected modes can be observed in figure 15(b). Subsequently, the subsurface notch in Region B is clearly identified and localized even in the presence of the vertical

stiffener in the collocation of the notch, as shown in figure 16(a). After denoising, only notch-reflected energy concentration is highlighted, as shown in figure 16(b).

6. Conclusion

This paper presents a WUWI technique for hidden damage detection inside a steel box girder bridge. The WUWI system and the corresponding damage visualization algorithm were developed, and their applicability to real structures were examined through full-scale field testing at the decommissioned Ramp-G Bridge in South Korea, which is a unique opportunity provided by Korea Expressway Corporation for performing destructive testing. The experimental results demonstrate that the proposed WUWI technique successfully visualizes only hidden cracks inside the steel box girder of the bridge without comparing them to baseline data even when the crack and an additional stiffener coexist.

However, the proposed technique as the very first trial for field bridge applications still has several implementation issues to be resolved. First, the precise laser aiming from an excitation unit to a target photodiode in a PZT excitation node and a photovoltaic panel can be a challenging task when the target bridge is exposed to vibration from traffic or wind loading. Although a manual aiming strategy is used in this study, it is envisioned that an automated aiming system such as a visual servoing system [27] can improve the applicability of the WUWI technique. Second, an LDV often requires time-domain averaging of responses with respect to each spatial sensing point to improve their signal-to-noise ratios. However, in-service bridges under noticeable vibration conditions make it difficult to retain multiple sensing at an identical spatial point. During the LDV measurement, the movement of the target point may disturb appropriate wavefield collection. Third, a special surface treatment such as retro-reflective tapes or paints might be necessary to enhance the LDV sensitivity on field bridge surface conditions. Finally, there can be an eye safety issue related to the use of high-power continuous CW lasers (Class 4). Further studies are warranted to address these issues.

Acknowledgement

References

[1] DeWolf J T and Bernard K J 1994 Fatigue failure investigation—Putnam Bridge *The final report of the Joint Highway Research Project JHR* 94–237

[2] Brownjohn J M W, Moyo P, Omenzetter P and Lu Y 2003 Assessment of highway bridge upgrading by dynamic testing and finite element model updating *J. Bridge Eng.* **8** 162–72

[3] Huth O, Feltrin G, Maeck J, Kilic N and Motavalli M 2005 Damage identification using modal data: experiences on a prestressed concrete bridge *J. Struct. Eng.* **131** 1898–910

[4] Lin X K, Zhang L M, Guo Q T and Zhang Y F 2009 Dynamic finite element model updating of prestressed concrete continuous box-girder bridge *Earthquake Eng. Eng. Vib.* **8** 399–407

[5] Chang P C, Flatau A and Liu S C 2003 Review paper: health monitoring of civil infrastructure *Struct. Health Monitoring* **2** 257–67

[6] Lynch J P 2007 An overview of wireless structural health monitoring for civil structures *Phil. Trans. R. Soc. Lond.* A **365** 345–72

[7] Salamone S, Bartoli I, Phillips R, Nucera C and Di Scalea F L 2011 Health monitoring of prestressing tendons in posttensioned concrete bridges *Transport. Res. Rec.* **2220** 21–7

[8] An Y-K, Lim H J, Kim M K, Yang J Y, Sohn H and Lee C G 2014 Investigation of applicability of local reference-free damage detection techniques to *in-situ* bridges *J. Struct. Eng.* **140** 04013069

[9] Nair A 2010 Acoustic emission monitoring of bridges: review and case studies *Eng. Struct.* **32** 1704–14

[10] Washer G A 1998 Developments for the non-destructive evaluation of highway bridges in the USA *NDT&E Int.* **31** 245–9

[11] Jiles D C, Hariharan S and Devine M K 1990 Magnescope: a portable magnetic inspection system for evaluation of steel structures and components *IEEE Trans. Magn.* **26** 2577–9

[12] Scruby C B and Drain L E 1990 *Laser Ultrasonics: Techniques and Applications* (London: Taylor and Francis)

[13] An Y-K, Park B and Sohn H 2013 Complete noncontact laser ultrasonic imaging for automated crack visualization in a plate *Smart Mater. Struct.* **22** 025022

[14] Park B, An Y-K and Sohn H 2014 Visualization of delamination and debonding in composites through noncontact laser scanning *Compos. Sci. Technol.* **100** 10–8

[15] Lynch J P 2007 An overview of wireless structural health monitoring for civil structures *Phil. Trans. R. Soc. Lond.* **365** 345–72

[16] Dove J R, Park G and Farrar C R 2006 Hardware design of hierarchal active-sensing networks for structural health monitoring *Smart Mater. Struct.* **15** 139–46

[17] Zhong C H, Croxford A J and Wilcox P D 2013 Investigation of inductively coupled ultrasonic transducer system for NDE *IEEE Trans. Ultrason. Ferroelec. Freq. Control* **60** 1115–25

[18] Park H-J, Sohn H, Yun C-B, Chung J and Lee M 2012 Wireless guided wave and impedance measurement using laser and piezoelectric transducers *Smart Mater. Struct.* **21** 035029

[19] An Y-K, Kwon Y and Sohn H 2013 Noncontact laser ultrasonic crack detection for plates with additional structural complexities *Struct. Health Monitoring* **12** 522–38

[20] Arns R G 1998 The other transistor: early history of the metal-oxide-semiconductor field-effect transistor *Eng. Sci. Educ. J.* **7** 233–40

[21] Wilson J and Hawkes J 1998 *Optoelectronics: An Introduction* (Englewood Cliffs, NJ: Prentice-Hall)

[22] Kasap S O 2001 *Optoelectronics and Photonics: Principles and Practices* (Englewood Cliffs, NJ: Prentice-Hall)

[23] http://www.polytec.com/

[24] Park H and Sohn H 2006 Parameter estimation of the generalized extreme value distribution for structural health monitoring *J. Prob. Eng. Mech.* **21** 366–76

[25] http://www.americanpiezo.com/

[26] Castaings M, Le Clezio E and Hosten B 2002 Modal decomposition method for modeling the interaction of Lamb waves with cracks *J. Acoust. Soc. Am.* **112** 2567–82

[27] Bang Y, Park J and Myung H 2011 Mobile robot-based visual targeting for wireless power transmission to WSN *World Congr. on Advances in Structural Engineering and Mechanics (Seoul, Sept)*